

Quantum randomness certification with untrusted measurements and few probe states

Kieran Neil Wilkinson,^{1,*} Casper Ahl Breum,¹ Tobias Gehring,¹ and Jonatan Bohr Brask¹

¹*Center for Macroscopic Quantum States (bigQ), Department of Physics, Technical University of Denmark, 2800 Kongens Lyngby, Denmark*

We present a scheme for quantum random-number generation from an untrusted measurement device and a trusted source and demonstrate it experimentally. No assumptions about noise or imperfections in the measurement are required, and the scheme is simple to implement with existing technology. The measurement device is probed with a few trusted states and the output entropy can be lower bounded conditioned on the observed outcome distribution. The protocol can be applied to measurements with any finite number of outcomes and in particular can be realised by homodyne measurements of the vacuum using a detector probed by coherent states, as we experimentally demonstrate by intensity modulation of a telecom-wavelength pilot laser followed by homodyne detection and discretisation by analog-to-digital conversion. We show that randomness can be certified in the presence of both Gaussian additive noise and non-Gaussian imperfections.

Random numbers are central to a range of applications in science and technology, including numerical simulation, statistical sampling, gaming, and secure information processing [1]. In particular, for cryptographic applications, security relies on the inability of any adversary to predict the random numbers used to generate cryptographic keys. To establish security, it is thus crucial to provide rigorous bounds on the predictability of the randomness used.

Within classical physics, such randomness certification necessarily relies on assumptions on the knowledge and computational resources available to potential eavesdroppers. The inherent randomness in measurements on quantum systems, on the other hand, allows certification to be based directly on measurable properties of the devices used, under the reasonable assumption that adversaries are also constrained by quantum physics [2–4]. Provided a characterisation of a quantum state and measurement – e.g. the output path of a single photon impinging on a beam splitter [5] – the predictability relative to any adversary can be bounded. Exploiting quantum nonlocality [6, 7], the need for accurate characterisation of the devices can even be eliminated, provided the measurement data violates a Bell inequality [8, 9]. This has been demonstrated experimentally [9–14] and provides a very strong level of security, known as device independence, since the devices may be largely untrusted.

However, device-independent schemes are also much more challenging to realise than simple device-dependent ones. It, therefore, makes sense to explore the trade-off between security and ease of implementation, identifying schemes that are fast and simple to realise at the price of introducing some limited amount of trust in the devices. Such protocols are broadly termed semi-device-independent, and many different setups with partially characterised state preparation or measurements have been considered, see e.g. [15–30]. One simple approach

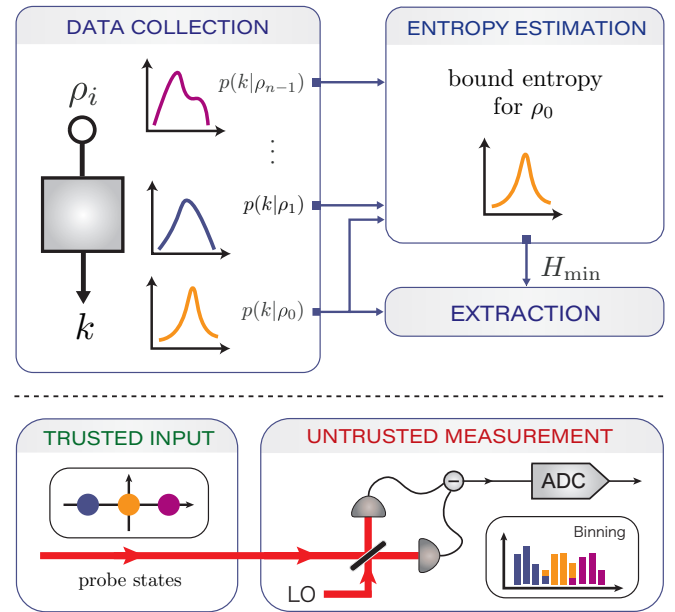


FIG. 1. Top: General protocol. An untrusted detector is probed with a set of trusted states and the distributions of outcomes are recorded. The min-entropy of the data corresponding to one of the states is lower bounded given the observations, and finally randomness extraction is applied. Bottom: implementation based on homodyning the vacuum. The generation and additional probe states are the vacuum and a set of coherent states with varying amplitude and fixed phase. The measurement is homodyne detection. The signal is discretised into $d = 2^\Delta$ bins by an ADC.

to quantum randomness generation, which can reach very high rates, is to extract randomness from optical quadrature measurements of the vacuum state [31–34]. This also allows for fast, source-device-independent schemes [23, 25], and security in settings with correlations across measurement rounds [35].

In this work, we first develop a method for randomness certification from a trusted source in prepare-and-measure setups, where the measurement is partially characterised using a small set of known input states. We

* Current address: Quantinuum, 17 Beaumont St, Oxford OX1 2NA

then apply our framework to homodyning of the vacuum in an optical setup and demonstrate this scheme in an experiment.

The method is illustrated in the upper panel of Fig. 1. A measurement device – initially an uncharacterised black box – is probed using a (small) set of known quantum states $\{\rho_0, \dots, \rho_{n-1}\}$, and the distributions $p(k|\rho_i)$ of outcomes are recorded. The entropy produced by measurements on a fixed state ρ_0 can be bounded via semidefinite programming using the observed data as constraints, without further assumptions about the behaviour or noise affecting the measurement device. This approach is general and applies to any prepare-and-measure scenario in which some input states may be trusted.

In the case of homodyne measurements of the vacuum, the fixed input is the vacuum state, and we take the remaining states to be coherent states with varying amplitude. The (untrusted) measurement is detection of a fixed quadrature, discretised by analogue-to-digital conversion to a finite number of outcomes. We show that significant min-entropy can be produced using just a few probe states, in the presence of both Gaussian and non-Gaussian noise. We note that the scheme operates far from the regime of detector tomography and already with the vacuum and a single coherent state, randomness can be extracted. Experimentally, we demonstrate our scheme in a simple optical setup with up to four probe states. In the following, we first describe the protocol and then our experimental implementation.

In general, the randomness relative to an adversary (Eve) can be quantified by how well Eve is able to predict the outcomes in generation rounds, i.e. by the guessing probability p_g that she correctly predicts the output k when the input is ρ_0 . By the left-over hash lemma, the asymptotic number of extractable random bits per round is then given by the min-entropy $H_{\min} = -\log_2 p_g$. We now show how p_g may be upper bounded (and hence H_{\min} lower bounded) by a semidefinite program (SDP).

The measurement device implements some unknown, noisy measurement. While the user observes only the average behaviour, we assume Eve has perfect knowledge of these measurements, which we associate with a d -outcome positive-operator-valued measure (POVM) $\hat{\Pi}_k^\lambda$. Here, λ labels the measurement strategies, which occur with distribution q_λ . For a particular POVM, the probability that Eve guesses correctly is determined by the most likely outcome $p_g = \max_k \text{Tr}[\rho_0 \hat{\Pi}_k^\lambda]$. An upper bound on p_g is then found by optimising over POVMs $\hat{\Pi}_k^\lambda$ and probability distributions q_λ , given the average observed behaviour

$$p_g \leq \min_{\{q_\lambda, \hat{\Pi}_k^\lambda\}} q_\lambda \max_k \text{Tr}[\rho_0 \hat{\Pi}_k^\lambda] \quad (1)$$

$$\text{s.t.} \quad \sum_\lambda q_\lambda \text{Tr}[\rho_i \hat{\Pi}_k^\lambda] = p(k|\rho_i) \quad \forall i, k.$$

This optimisation is not yet an SDP as it is nonlin-

ear in $\hat{\Pi}_k^\lambda$ and q_λ and contains the maximisation over k . The latter issue can be resolved by observing that, while the number of strategies available to Eve is a priori unlimited, following the logic of Ref. [36], all strategies for which the most likely k in (1) is the same can be grouped together. Thus we need only consider d different POVMs, and we can let λ label the optimal k , i.e. $\max_k \text{Tr}[\rho_0 \hat{\Pi}_k^\lambda] = \text{Tr}[\rho_0 \hat{\Pi}_\lambda^\lambda]$. The problem can now be linearised by introducing new variables $\hat{M}_k^\lambda = q_\lambda \hat{\Pi}_k^\lambda$. We obtain

$$p_g = \max_{\{\hat{M}_k^\lambda\}} \sum_{\lambda=1}^d \text{Tr}[\rho_0 \hat{M}_\lambda^\lambda]$$

$$\text{s.t.} \quad \hat{M}_k^\lambda \geq 0 \quad \forall k, \lambda$$

$$\sum_{k=1}^d \hat{M}_k^\lambda = \frac{1}{D} \text{Tr} \left[\sum_k \hat{M}_k^\lambda \right] \mathbb{I} \quad \forall \lambda \quad (2)$$

$$\sum_{\lambda=1}^d \text{Tr}[\rho_i \hat{M}_k^\lambda] = p(k|\rho_i) \quad \forall i, k$$

which is an SDP. Here, D is the dimension of the POVM elements, and the first two constraints ensure that the \hat{M}_k^λ form a valid POVM and the q_λ a valid probability distribution. Note while ideally we do not want to constrain the dimension, when implementing the SDP, D must be finite. D should thus be chosen sufficiently large to not affect the optimum. Also note that in practice, it is often more useful to work with the dual SDP, in which the observed data enters in the objective function and not in the constraints. We derive the dual in App. A.

Next, we apply our scheme to the particular case of homodyning the vacuum and probing with coherent states. We will model both additive Gaussian noise in the measurement and non-Gaussian noise from the analogue-to-digital converter (ADC), in order to compute how much randomness one may expect to extract from such a protocol. We stress, however, that in bounding the entropy, no assumptions are made about the particular form of the noise or the measurement.

The setup is illustrated in the lower panel of Fig. 1. The trusted input states are $\rho_0 = |0\rangle\langle 0|$ and $\rho_i = |\alpha_i\rangle\langle \alpha_i|$, with α_i real, i.e. along the X -quadrature. We take the untrusted measurement to be of the X -quadrature, binned by a Δ -bit ADC to give $d = 2^\Delta$ outcomes. In the absence of imperfections, the measurement before binning is a projection $|x\rangle\langle x|$ onto quadrature eigenstates. To include noise, we consider a Gaussian distribution of variance σ_n^2 and mean x that converts the projector $|x\rangle\langle x|$ into a POVM element

$$\hat{\Sigma}_x = \int_{-\infty}^{\infty} |y\rangle\langle y| \frac{\exp[-(y-x)^2/2\sigma_n^2]}{\sqrt{2\pi}\sigma_n} dy. \quad (3)$$

The noise strength is thus determined by σ_n and can be stated in terms of the signal-to-noise ratio (SNR) σ_v^2/σ_n^2 , where σ_v^2 is the vacuum variance. The noise is additive

as the observed variance for a Gaussian input state with variance σ_v^2 becomes $\sigma_v^2 + \sigma_n^2$. We also account for a detection efficiency η (which transforms $\alpha_i \rightarrow \sqrt{\eta}\alpha_i$ in the calculation of the outcome distributions).

The ADC bins continuous outcomes into $d = 2^\Delta$ intervals I_k , where k labels the corresponding outputs. For an ideal ADC, the POVM elements thus become

$$\hat{\Sigma}_k = \int_{I_k} \hat{\Sigma}_x dx, \quad (4)$$

with $\hat{\Sigma}_x$ given by (3). Commonly, the I_k are $d-2$ adjacent bins of equal width that span a range R on both sides of a central point in the X -quadrature. The remaining two end bins cover the values below and above this range. Mathematically, we have

$$I_k = \begin{cases} (-\infty, -R] & \text{if } k = 0 \\ [a_k - \delta/2, a_k + \delta/2) & \text{if } k = 1, \dots, d-2 \\ (R, \infty) & \text{if } k = d-1 \end{cases} \quad (5)$$

where $a_k = -R + (2k-1)\delta/2$ and $\delta = 2R/(d-2)$ is the bin width. A priori, for randomness generation from the vacuum, a uniform distribution over k is desired and the bin widths should then vary with k , since the corresponding X -quadrature distribution is a Gaussian. However, this is not always optimal here where additional probe states are also considered. Moreover, it is difficult to implement with standard ADCs, and thus less relevant experimentally. For completeness, in Apps. B and C we do consider varying bin widths as well as a setting where the average detector POVM is completely known (i.e. the limit where the set of probe states is tomographically complete).

Modern ADCs achieve high speeds by interleaving several individual ADC units in time. This can lead to a non-Gaussian noise effect where the weights of adjacent even and odd bins become imbalanced. We model the corresponding POVM as

$$\hat{\Sigma}_k^\gamma = \begin{cases} \hat{\Sigma}_k + \gamma \hat{\Sigma}_{k+1} & (k \text{ even}) \\ (1-\gamma)\hat{\Sigma}_k & (k \text{ odd}) \end{cases} \quad (6)$$

which can be understood as follows. For each odd bin, a fraction γ of events corresponding to this outcome are shifted to the neighbouring even bin above. Given this model of the imperfect measurement device, we can compute the outcome distributions $p(k|\rho_i)$ needed in the SDP (2). We have

$$p^\gamma(k|\alpha) = \begin{cases} p(k|\alpha) + \gamma p(k+1|\alpha) & (k \text{ even}) \\ (1-\gamma)p(k|\alpha) & (k \text{ odd}) \end{cases} \quad (7)$$

where, as shown in App. B,

$$p(k|\alpha) = \text{Tr} \left[|\alpha\rangle \langle \alpha| \hat{\Sigma}_k \right] \quad (8)$$

$$= \frac{1}{2} \text{erf} [v(b_k)] - \frac{1}{2} \text{erf} [v(a_k)], \quad (9)$$

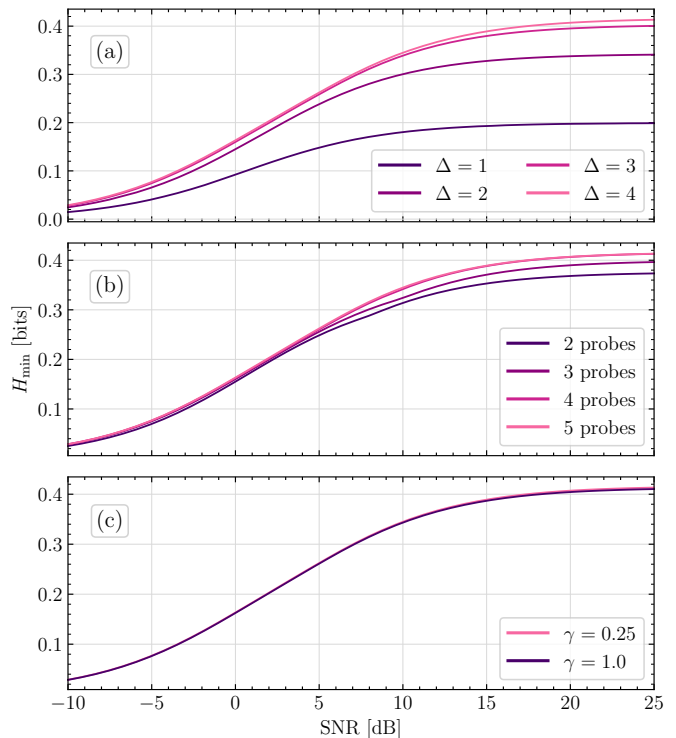


FIG. 2. Results from modeling the protocol. The min-entropy is shown vs. the signal-to-noise ratio of the Gaussian noise, for varying parameter settings. **(a)** varying $\Delta = 1, 2, 3, 4$ (bottom to top) with fixed $\gamma = 0.25$, $\eta = 0.9$, 5 probe states with amplitudes equally spaced between 0 and a maximum value $\bar{\alpha}$ which, as well as R , is optimized at each SNR. **(b)** Fixed $\gamma = 0.25$, $\eta = 0.9$, $\Delta = 4$ with optimal R and $\bar{\alpha}$, and varying number of probe states 2,3,4,5 (bottom to top). **(c)** Fixed $\eta = 0.9$, $\Delta = 4$, 5 probe states, optimal R and $\bar{\alpha}$, and varying $\gamma = 0.25, 1$ (top to bottom).

where a_k and b_k are the lower and upper boundaries of I_k , respectively, and $v(x) = (x - \sqrt{2}\alpha)/(\sqrt{2}\sigma_t)$ where σ_t is the standard deviation of the total noise (vacuum and excess Gaussian noise).

The results for randomness certification are shown in Fig. 2. We see that while the randomness degrades with very strong additive noise (low SNR), for reasonable noise at the 10% level, the protocol performs well and the entropy starts to saturate. From Fig. 2(a), we see that, as may be expected, more randomness can be certified with a larger number of outputs but saturates with increasing Δ . For the parameter settings considered here, the additional gain above $\Delta = 4$ (16 outputs) is minor [37]. From Fig. 2(b), we see that a similar behaviour applies to the number of trusted states. Notably, already with two states (i.e. the vacuum and a single coherent state), randomness can be certified with $H_{\min} \approx 0.35$ in a low-noise scenario. In the ideal case with $\Delta = 4$, probe state amplitudes $\{0, \alpha\}$ we obtain $H_{\min} = 0.499$ with optimal values $R = 1.80$ and $\alpha = -1.68 \times 10^{-4}$. Finally, from Fig. 2(c) we see that the protocol is very robust against the non-Gaussian ADC noise. Even for $\gamma = 1$, where ev-

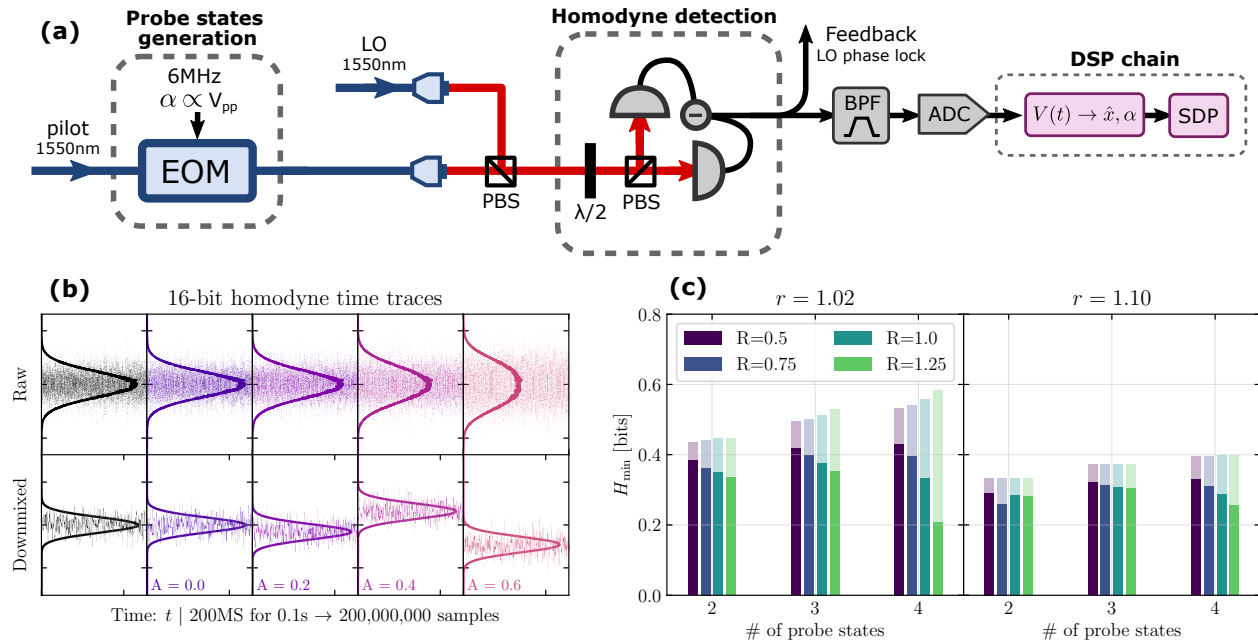


FIG. 3. (a) Experimental setup. Probe states, created as sideband states by amplitude modulating a pilot beam with an EOM, are measured by balanced homodyne detection. The photocurrent is bandpass filtered (BPF) around the modulation frequency before being converted to bit values by an ADC. The resulting time traces are then processed by a 2-block digital signal processing (DSP) chain. (b) Time traces collected for a single data set overlain with equally-scaled histograms of the bit value distributions. For the raw time traces, the vertical axis spans the entire ADC range: $[-2^{15}, 2^{15}]$, while for the downmixed time traces we zoom to the middle half. (c) Experimental min-entropy for various DSP settings. We perform downsampling with bit depth $\Delta = 6$ and various ADC ranges R . The faded histograms show the min-entropy in the ideal case of infinite data, while the overlaid solid histograms show the entropy after accounting for finite-size effects. To handle uncertainty in the estimation of the probe state amplitudes, we consider two values of the scaling parameter r equivalent to assuming the amplitudes are 2% (left) and (10% (right) larger than the estimated values (see App. F 4).

ery second bin is effectively removed, the entropy barely degrades in the optimal regime.

Next, we experimentally demonstrate the performance of the protocol using the setup outlined in Fig. 3(a) (for a more detailed figure and explanation see App. F). Probe states are generated as sideband states by intensity modulating a pilot beam at $f_{\text{mod}} = 6$ MHz with an electro-optic modulator (EOM). The peak-to-peak voltage V_{pp} used to drive the EOM is well below the corresponding half-wave voltage of the EOM, thus the amplitudes α of the sideband states are directly proportional to V_{pp} . In a single data set we collect five time traces: a shot-noise trace (corresponding to vacuum), where the pilot beam is blocked, and four traces with $A = 0.0, 0.2, 0.4, 0.6$, where A indicates the scaling of V_{pp} . The pilot beam is then directly measured by a polarization-based homodyne detector and the resulting photo-current is bandpass filtered (BPF) around f_{mod} before being recorded by a 16-bit ADC. The homodyne detector also has a lower-bandwidth DC output, which is used to generate an error signal to lock the phase between the LO and pilot beam, such that the X -quadrature is measured. The bit value distributions $V(t)$, as recorded by the ADC of five such traces, are shown in the top row of Fig. 3(b). In order to optimise the certifiable randomness, the LO power

and ADC range was tuned such that the shot noise trace spans the entire ADC range. The traces were recorded with an estimated total detection efficiency of at least 90%, with inefficiency stemming from propagation loss between the EOM and homodyne detector, imperfect visibility between pilot and LO and the quantum efficiency of the homodyne detector diodes.

After the ADC, the data set goes through a digital signal processing (DSP) chain consisting of two blocks. In the first block, the X -quadrature distributions of the sideband probe states are extracted from the raw time traces and their corresponding amplitudes estimated. This is done in four steps: digital downmixing, shot noise normalization, amplitude estimation and downsampling, which are all described in detail in App. F 1. The result of the first of these steps $V_{\text{dm}}(t)$ is shown in the bottom row of Fig. 3(b). In the second block, the observed distributions and estimated amplitudes are used to compute a bound on the entropy of the measured data from the vacuum input via SDP, as described above. Specifically, the trusted states in the SDP constraints are coherent states based on the estimated amplitudes and the observed distribution is given by the normalized histograms from the experiment. The result of this is shown in Fig. 3(c). In order to avoid estimation errors compromising the secu-

rity, we scale our estimations of the amplitudes according to $\alpha_i = r\alpha_i^{\text{true}}$ with $r > 1$, thus making the trusted states more distinguishable and decreasing the certifiable randomness (see App. G). Additionally, we account for finite-size effects on the output entropy (see App. E1).

The results presented in Fig. 3(c) show that a considerable amount of randomness can be generated using our protocol with a relatively small number of probe states after accounting for both amplitude estimation errors and finite-size effects. We observe that, in the case of low estimation errors and ignoring finite-size effects, the minimum entropy increases with R . However, the finite-size correction also increases with R , eliminating the advantage in most cases. Nevertheless, even with 10% estimation errors the entropy per round remains above 0.25.

In summary, we have demonstrated a protocol for semi-device-independent randomness certification that is sim-

ple to implement yet highly robust and secure. The entropy can be bounded online (interleaving generation and additional probe rounds), allowing continuous self-testing operation. It would be interesting to extend the security proof to probe states correlated with Eve (mixed states). Finally, it would be interesting to investigate if our general scheme can be applied to existing device-dependent QRNG protocols to help strengthen security, or extended to key distribution.

ACKNOWLEDGMENTS

We gratefully acknowledge support from the Danish National Research Foundation, Center for Macroscopic Quantum States (bigQ, DNRF142), the Carlsberg Foundation CF19-0313 and CF21-0466, and the Independent Research Fund Denmark 7027-00044B and 0171-00055B.

-
- [1] B. Hayes, Randomness as a resource, *American Scientist* **89**, 300 (2001).
 - [2] A. Acín and L. Masanes, Certified randomness in quantum physics, *Nature* **540**, 213 (2016).
 - [3] M. Herrero-Collantes and J. C. Garcia-Escartin, Quantum random number generators, *Rev. Mod. Phys.* **89**, 015004 (2017).
 - [4] M. Bera, A. Acín, M. Kus, M. Mitchell, and M. Lewenstein, Randomness in Quantum Mechanics: Philosophy, Physics and Technology, *Rep. Prog. Phys.* **80**, 124001 (2017).
 - [5] A. Stefanov, N. Gisin, O. Guinnard, L. Guinnard, and H. Zbinden, Optical quantum random number generator, *J. Mod. Opt.* **47**, 595 (2000).
 - [6] J. Bell, On the einstein podolsky rosen paradox, *Physics* **1**, 195 (1964).
 - [7] N. Brunner, D. Cavalcanti, S. Pironio, V. Scarani, and S. Wehner, Bell nonlocality, *Rev. Mod. Phys.* **86**, 419 (2014).
 - [8] R. Colbeck, Quantum and relativistic protocols for secure multi-party computation, Ph.D. Thesis, University of Cambridge (2009), arXiv:0911.3814 [quant-ph].
 - [9] S. Pironio, A. Acín, S. Massar, A. B. de la Giroday, D. N. Matsukevich, P. Maunz, S. Olmschenk, D. Hayes, L. Luo, T. A. Manning, and C. Monroe, Random numbers certified by bell's theorem, *Nature* **464**, 1021 (2010).
 - [10] B. G. Christensen, K. T. McCusker, J. B. Altepeter, B. Calkins, T. Gerrits, A. E. Lita, A. Miller, L. K. Shalm, Y. Zhang, S. W. Nam, N. Brunner, C. C. W. Lim, N. Gisin, and P. G. Kwiat, Detection-loophole-free test of quantum nonlocality, and applications, *Phys. Rev. Lett.* **111**, 130406 (2013).
 - [11] P. Bierhorst, E. Knill, S. Glancy, Y. Zhang, A. Mink, S. Jordan, A. Rommal, Y.-K. Liu, B. Christensen, S. W. Nam, M. J. Stevens, and L. K. Shalm, Experimentally Generated Randomness Certified by the Impossibility of Superluminal Signals, *Nature* **556**, 223 (2018).
 - [12] Y. Liu, Q. Zhao, M.-H. Li, J.-Y. Guan, Y. Zhang, B. Bai, W. Zhang, W.-Z. Liu, C. Wu, X. Yuan, H. Li, W. J. Munro, Z. Wang, L. You, J. Zhang, X. Ma, J. Fan, Q. Zhang, and J.-W. Pan, Device-independent quantum random-number generation, *Nature* **562**, 548 (2018).
 - [13] L. K. Shalm, Y. Zhang, J. C. Bienfang, C. Schlager, M. J. Stevens, M. D. Mazurek, C. Abellán, W. Amaya, M. W. Mitchell, M. A. Alhejji, H. Fu, J. Ornstein, R. P. Mirin, S. W. Nam, and E. Knill, Device-independent randomness expansion with entangled photons, *Nature Physics* **17**, 452 (2021).
 - [14] W.-Z. Liu, M.-H. Li, S. Ragy, S.-R. Zhao, B. Bai, Y. Liu, P. J. Brown, J. Zhang, R. Colbeck, J. Fan, Q. Zhang, and J.-W. Pan, Device-independent randomness expansion against quantum side information, *Nature Physics* **17**, 448 (2021).
 - [15] H.-W. Li, Z.-Q. Yin, Y.-C. Wu, X.-B. Zou, S. Wang, W. Chen, G.-C. Guo, and Z.-F. Han, Semi-device-independent random-number expansion without entanglement, *Phys. Rev. A* **84**, 034301 (2011).
 - [16] G. Vallone, D. G. Marangon, M. Tomasin, and P. Villoresi, Quantum randomness certified by the uncertainty principle, *Phys. Rev. A* **90**, 052327 (2014).
 - [17] T. Lunghi, J. B. Brask, C. C. W. Lim, Q. Lavigne, J. Bowles, A. Martin, H. Zbinden, and N. Brunner, Self-testing quantum random number generator, *Phys. Rev. Lett.* **114**, 150501 (2015).
 - [18] A. Chaturvedi and M. Banik, Measurement-device-independent randomness from local entangled states, *EPL (Europhysics Letters)* **112**, 30003 (2015).
 - [19] Z. Cao, H. Zhou, and X. Ma, Loss-tolerant measurement-device-independent quantum random number generation, *New J. Phys.* **17**, 125011 (2015).
 - [20] Y.-Q. Nie, J.-Y. Guan, H. Zhou, Q. Zhang, X. Ma, J. Zhang, and J.-W. Pan, Experimental measurement-device-independent quantum random-number generation, *Phys. Rev. A* **94**, 060301 (2016).
 - [21] Z. Cao, H. Zhou, X. Yuan, and X. Ma, Source-Independent Quantum Random Number Generation, *Phys. Rev. X* **6**, 011020 (2016).
 - [22] F. Xu, J. H. Shapiro, and F. N. C. Wong, Experimen-

- tal fast quantum random number generation using high-dimensional entanglement with entropy monitoring, *Optica* **3**, 1266 (2016).
- [23] D. G. Marangon, G. Vallone, and P. Villoresi, Source-device-independent ultrafast quantum random number generation, *Phys. Rev. Lett.* **118**, 060503 (2017).
- [24] J. B. Brask, A. Martin, W. Esposito, R. Houlmann, J. Bowles, H. Zbinden, and N. Brunner, Megahertz-Rate Semi-Device-Independent Quantum Random Number Generators Based on Unambiguous State Discrimination, *Phys. Rev. Appl.* **7**, 054018 (2017).
- [25] M. Avesani, D. G. Marangon, G. Vallone, and P. Villoresi, Source-device-independent heterodyne-based quantum random number generator at 17 gbps, *Nature Communications* **9**, 5365 (2018).
- [26] T. Michel, J. Y. Haw, D. G. Marangon, O. Thearle, G. Vallone, P. Villoresi, P. K. Lam, and S. M. Assad, Real-time source-independent quantum random-number generator with squeezed states, *Phys. Rev. Applied* **12**, 034017 (2019).
- [27] D. Rusca, T. van Himbeek, A. Martin, J. B. Brask, W. Shi, S. Pironio, N. Brunner, and H. Zbinden, Self-testing quantum random-number generator based on an energy bound, *Phys. Rev. A* **100**, 062338 (2019).
- [28] D. Drahı, N. Walk, M. J. Hoban, A. K. Fedorov, R. Shakhovoy, A. Feimov, Y. Kurochkin, W. S. Kolthammer, J. Nunn, J. Barrett, and I. A. Walmsley, Certified quantum random numbers from untrusted light, *Phys. Rev. X* **10**, 041048 (2020).
- [29] D. Rusca, H. Tebyanian, A. Martin, and H. Zbinden, Fast self-testing quantum random number generator based on homodyne detection, *Applied Physics Letters* **116**, 264004 (2020).
- [30] P. Mironowicz, G. Cañas, J. Cariñe, E. S. Gómez, J. F. Barra, A. Cabello, G. B. Xavier, G. Lima, and M. Pawłowski, Quantum randomness protected against detection loophole attacks, *Quantum Information Processing* **20**, 39.
- [31] C. Gabriel, C. Wittmann, D. Sych, R. Dong, W. Mauerer, U. L. Andersen, C. Marquardt, and G. Leuchs, A generator for unique quantum random numbers based on vacuum states, *Nature Photonics* **4**, 711 (2010).
- [32] T. Symul, S. M. Assad, and P. K. Lam, Real time demonstration of high bitrate quantum random number generation with coherent laser light, *Applied Physics Letters* **98**, 231103 (2011).
- [33] X.-G. Zhang, Y.-Q. Nie, H. Zhou, H. Liang, X. Ma, J. Zhang, and J.-W. Pan, Note: Fully integrated 3.2 gbps quantum random number generator with real-time extraction, *Review of Scientific Instruments* **87**, 076102 (2016).
- [34] L. Huang and H. Zhou, Integrated gbps quantum random number generator with real-time extraction based on homodyne detection, *J. Opt. Soc. Am. B* **36**, B130 (2019).
- [35] T. Gehring, C. Lupo, A. Kordts, D. Solar Nikolic, N. Jain, T. Rydberg, T. B. Pedersen, S. Pirandola, and U. L. Andersen, Homodyne-based quantum random number generator at 2.9 gbps secure against quantum side-information, *Nature Communications* **12**, 605 (2021).
- [36] J.-D. Bancal, L. Sheridan, and V. Scarani, More randomness from the same data, *New Journal of Physics* **16**, 033011 (2014).
- [37] We note that, in the absence of noise and for a tomographically complete set of probe states (or equivalently a fully characterised POVM), the certifiable randomness will be Δ bits. However, the coherent-state probes considered here are not tomographically complete and even for a complete set, convergence towards maximal randomness with SNR is slow.
- [38] W. Hoeffding, Probability inequalities for sums of bounded random variables, *Journal of the American Statistical Association* **58**, 13 (1963).

Appendix A: Dual SDP

Here, we derive the dual of the SDP given in the main text for computing the guessing probability. The dual SDP does not feature the observed data in its constraints, only in the objective function and the solution provides an upper bound on the guessing probability for any set of data. As a result, the set of optimal parameters obtained by solving the dual problem for one set of data may be used to upper-bound the guessing probability for any other set of data by straightforward evaluation of the objective function.

Firstly, recall the set of primal constraints (c.f. (2) in the main text):

$$\hat{M}_k^\lambda \geq 0 \quad \forall k, \lambda \in \{1, \dots, d\} \quad (\text{A1})$$

$$\sum_{k=1}^d \hat{M}_k^\lambda = \frac{1}{D} \text{Tr} \left[\sum_k \hat{M}_k^\lambda \right] \mathbb{I} \quad \forall \lambda \in \{1, \dots, d\}, \quad (\text{A2})$$

$$\sum_{\lambda=1}^d \text{Tr} \left[\rho_i \hat{M}_k^\lambda \right] = p(k|\rho_i) \quad \forall i \in \{1, \dots, n\}, k \in \{1, \dots, d\}. \quad (\text{A3})$$

We begin by introducing a dual variable for each of the constraints above. For those defined by (A1), we introduce semi-definite matrices $\{G_k^\lambda\}$. Similarly, for those defined by (A2) we introduce semi-definite matrices $\{H_\lambda\}$. Finally, for the constraints defined by (A3), we introduce scalar variables $\{\nu_k^i\}$. Using these variables we form a Lagrangian from the sum of the primal objective function and, for each constraint, the product of the dual variable and the

difference between the left- and right-hand side of the constraint. We obtain

$$\mathcal{L} = \sum_{\lambda} \text{Tr} \left[\rho_0 \hat{M}_{\lambda}^{\lambda} \right] \quad (\text{A4})$$

$$+ \sum_{k,\lambda} \text{Tr} \left[G_k^{\lambda} \hat{M}_k^{\lambda} \right] \quad (\text{A5})$$

$$+ \sum_{\lambda} \text{Tr} \left[H_{\lambda} \left(\sum_k \hat{M}_k^{\lambda} - \frac{1}{D} \text{Tr} \left[\sum_k \hat{M}_k^{\lambda} \right] \mathbb{I} \right) \right] \quad (\text{A6})$$

$$+ \sum_{k,i} \nu_k^i \left(\sum_{\lambda} \text{Tr} \left[\rho_i \hat{M}_k^{\lambda} \right] - p(k|\rho_i) \right). \quad (\text{A7})$$

Note that the last two terms vanish when the primal variables fulfill the primal constraints. Hence, maximising \mathcal{L} provides an upper bound on p_g , if the $\{G_k^{\lambda}\}$ are chosen to be positive. Now, we group all terms in which the primal SDP variables $\{\hat{M}_k^{\lambda}\}$ appear, thus we obtain

$$\mathcal{L} = \sum_{\lambda,k} \text{Tr} \left[\hat{M}_k^{\lambda} K_k^{\lambda} \right] - \sum_{k,i} \nu_k^i p(k|\rho_i), \quad (\text{A8})$$

where we define

$$K_k^{\lambda} := \rho_0 \delta_{k,\lambda} + G_k^{\lambda} + H_{\lambda} - \frac{1}{D} \text{Tr} [H_{\lambda}] \mathbb{I} + \sum_{i=1}^n \nu_k^i \rho_i. \quad (\text{A9})$$

Let \mathcal{S} be the (unconstrained) supremum of the Lagrangian over the primal variables

$$\mathcal{S} = \sup_{\{\hat{M}_k^{\lambda}\}} \mathcal{L}. \quad (\text{A10})$$

One sees that, unless the $\{K_k^{\lambda}\}$ vanish, the supremum will diverge. Hence, to get a nontrivial upper bound, we demand that $K_k^{\lambda} = 0$. Since the $\{G_k^{\lambda}\}$ are positive but otherwise arbitrary, this is equivalent to the condition

$$\rho_0 \delta_{k,\lambda} + H_{\lambda} - \frac{1}{D} \text{Tr} [H_{\lambda}] \mathbb{I} + \sum_{i=1}^n \nu_k^i \rho_i \leq 0. \quad (\text{A11})$$

We thus arrive at the dual SDP by minimising the supremum

$$\begin{aligned} \bar{p}_g = \min_{\{H_{\lambda}\}, \{\nu_k^i\}} & - \sum_{k=1}^d \sum_{i=1}^n \nu_k^i p(k|\rho_i) \\ \text{s.t.} & H_{\lambda} = H_{\lambda}^{\dagger} \quad \forall \lambda, \\ & \rho_0 \delta_{k,\lambda} + H_{\lambda} - \frac{1}{D} \text{Tr} [H_{\lambda}] \mathbb{I} + \sum_{i=1}^n \nu_k^i \rho_i \leq 0 \quad \forall \lambda, k, \end{aligned} \quad (\text{A12})$$

where the dual optimum bounds the primal as $p_g \leq \bar{p}_g$.

Appendix B: Noisy, discretized measurement of a coherent state in the X -quadrature

Here, we derive the probabilities associated with measuring the X -quadrature of a coherent state with homodyne detection subject to Gaussian excess noise followed by binning. Our starting point is the X -quadrature wavefunction of the coherent state of (generally complex) amplitude α , given by

$$\psi_{\alpha}(x) = \frac{1}{\pi^{1/4}} \exp \left[-\frac{1}{2} \left(x - \sqrt{2} \Re(\alpha) \right)^2 + ix \sqrt{2} \Im(\alpha) \right] \quad (\text{B1})$$

where $\Re(\alpha)$ and $\Im(\alpha)$ are the real and imaginary parts of α , respectively. Recalling the form of the average POVM operators from (4), we may compute the probabilities as

$$p(k|\alpha) = \langle \alpha | \hat{\Sigma}_k | \alpha \rangle = \langle \alpha | \int_{I_k} \int_{-\infty}^{\infty} |y\rangle \langle y| \frac{\exp[-(y-x)^2/2\sigma_n^2]}{\sqrt{2\pi}\sigma_n} dy dx | \alpha \rangle \quad (\text{B2})$$

$$= \int_{I_k} \int_{-\infty}^{\infty} \frac{\exp[-(y-x)^2/2\sigma_n^2]}{\sqrt{2\pi}\sigma_n} |\psi_\alpha(y)|^2 dy dx \quad (\text{B3})$$

$$= \int_{I_k} \frac{1}{\sqrt{2\pi}\sigma_t} \exp\left[-\frac{(x - \sqrt{2}\Re(\alpha))^2}{2\sigma_t^2}\right] dx \quad (\text{B4})$$

$$= \frac{1}{2} \left[\operatorname{erf}\left(\frac{b_k - \sqrt{2}\Re(\alpha)}{\sqrt{2}\sigma_t}\right) - \operatorname{erf}\left(\frac{a_k - \sqrt{2}\Re(\alpha)}{\sqrt{2}\sigma_t}\right) \right] \quad (\text{B5})$$

where a_k (b_k) is the lower (upper) bound of the interval I_k , and $\sigma_t^2 = \sigma_v^2 + \sigma_n^2$ is the total variance of the output distribution in the X -quadrature before binning.

Appendix C: Complete detector tomography

In the protocol discussed in the main text, a black-box measurement device is probed using a small set of trusted states. An alternative (more demanding) approach is to perform full tomography of the detector (e.g. by using a tomographically complete set of probe states). This imposes stronger constraints on Eve and hence allows more randomness to be certified. In this approach, in the SDP (2), the constraints

$$\sum_{\lambda=1}^d \operatorname{Tr}[\rho_i \hat{M}_k^\lambda] = p(k|\rho_i) \quad \forall i, k, \quad (\text{C1})$$

would be replaced by

$$\sum_{\lambda=1}^d \hat{M}_k^\lambda = \hat{\Sigma}_k \quad \forall k, \quad (\text{C2})$$

where $\hat{\Sigma}_k$ is the observed POVM element for outcome k . We note that the dual problem in this case is given by

$$\begin{aligned} \bar{p}_g = \min_{\{H_\lambda\}, \{J_k\}} & - \sum_k \operatorname{Tr}[J_k \hat{\Sigma}_k] \\ \text{s.t.} & H_\lambda = H_\lambda^\dagger \quad \forall \lambda, \\ & J_k = J_k^\dagger \quad \forall k, \\ & \rho_0 \delta_{k,\lambda} + H_\lambda - \frac{1}{D} \operatorname{Tr}[H_\lambda] \mathbb{I} + J_k \leq 0 \quad \forall \lambda, k \end{aligned} \quad (\text{C3})$$

where each of $\{H_\lambda\}$ and $\{J_k\}$ are semi-definite matrices.

For a theoretical analysis of such a protocol based on homodyne detection of the vacuum, one needs to compute the expected $\hat{\Sigma}_k$ (in a similar manner as Fig. 2 of the main text was obtained from the expected distributions $p^\gamma(k|\alpha)$). For completeness, we provide a derivation of the $\{\hat{\Sigma}_k\}$ in Fock space for noisy homodyne detection and briefly outline numerical results which we compare to those obtained with the coherent state characterization approach.

1. Fock-space POVM elements of noisy homodyne detection

In this section we will derive the form of the noisy and discretized measurement operators $\hat{\Sigma}_k$ that we would expect a legitimate noisy homodyne detector and ADC to perform. In the ideal case, homodyne detection is a projective measurement on the X -quadrature with operators of the form $|x\rangle\langle x|$. Starting from the ideal measurement operator, we will derive the generic POVM element by first incorporating excess Gaussian noise and then allowing for discretization by an ADC with arbitrary bin boundaries.

a. *Gaussian excess noise*

Here, we will derive an analytic expression for the POVM element of a homodyne detection subject to Gaussian additive noise as expressed in (3), labeled $\hat{\Sigma}_x$. The generic Fock-space matrix element indexed by (μ, ν) of this measurement operator can be obtained as

$$(\hat{\Sigma}_x)_{\mu, \nu} = \langle \mu | \hat{\Sigma}_x | \nu \rangle = \langle \mu | \int_{-\infty}^{\infty} |y\rangle \langle y| \Pr[Y = y] dy | \nu \rangle \quad (C4)$$

$$= \int_{-\infty}^{\infty} \Pr[Y = y] \phi_{\mu}(y) \phi_{\nu}(y) dy. \quad (C5)$$

Here, the random variable $Y \sim \mathcal{N}(x, \sigma_n^2)$ is a normal distribution of mean x and variance σ_n^2 describing the additive Gaussian noise and $\Pr[Y = y]$ is the probability that Y takes the value y . The function $\phi_k(x) = \langle x | k \rangle$ is the X -quadrature wavefunction of a k -photon Fock state, given by

$$\phi_k(x) = \frac{1}{\sqrt{2^k k!}} \phi_0(x) H_k(x), \quad (C6)$$

where $H_k(x)$ is the k th Hermite polynomial defined by

$$H_k(x) = k! \sum_{n=0}^{\lfloor k/2 \rfloor} \frac{(-1)^n}{n!(k-2n)!} (2x)^{k-2n} \quad (C7)$$

and $\phi_0(x) = \pi^{-1/4} \exp(-x^2/2)$ is the wavefunction of the vacuum state where the variance of the vacuum fluctuations is normalized to $\sigma_v^2 = 1/2$. Using these definitions we can write an expression for a generic matrix element of a POVM element as

$$(\hat{\Sigma}_x)_{\mu, \nu} = \sqrt{\frac{\mu! \nu!}{2^{\mu+\nu}}} \sum_{m=0}^{\lfloor \mu/2 \rfloor} \sum_{n=0}^{\lfloor \nu/2 \rfloor} \frac{(-1)^{m+n} 2^{\mu+\nu-2m-2n}}{m! n! (\mu-2m)! (\nu-2n)!} \chi_{\mu+\nu-2m-2n}(x, \sigma_n^2) dy. \quad (C8)$$

where we define

$$\chi_n(x, \sigma_n^2) := \int_{-\infty}^{\infty} \frac{\exp[-y^2 - (y-x)^2/2\sigma_n^2]}{\sqrt{2\pi}\sigma_n} y^n dy \quad (C9)$$

$$= \frac{\exp[-x^2/2\sigma_t^2]}{\sqrt{2\pi}\sigma_t} \left(\frac{\sigma_N}{\sigma_t}\right)^n \frac{1}{2^n} \sum_{\nu=0}^{\lfloor n/2 \rfloor} \frac{n!}{\nu!(n-2\nu)!} \left(\frac{x}{\sigma_n \sigma_t}\right)^{n-2\nu} \quad (C10)$$

where $\sigma_t^2 = \sigma_v^2 + \sigma_n^2$. Observation that the sum on the right-hand side of the above expression is closely related to the Hermite polynomials allows for the efficient computation of consecutive matrix elements with recursion.

b. *ADC discretization*

Let us now include discretisation by an ADC. With reference to the operators described above, the generic matrix element (μ, ν) of the generic POVM element $\hat{\Sigma}_k$ is given by

$$(\hat{\Sigma}_k)_{\mu, \nu} = \int_{I_k} (\hat{\Sigma}_x)_{\mu, \nu} dx. \quad (C11)$$

Observation of (C8) reveals that the dependence on x is contained entirely within the function χ , hence we can concentrate on integrating this function for a general n . Let us define the following function

$$\tilde{\chi}_n(k, \sigma_n^2) = \int_{I_k} \chi_n(x, \sigma_n^2) dx \quad (C12)$$

$$= \frac{1}{\sqrt{2\pi}\sigma_t} \left(\frac{\sigma_N}{\sigma_t}\right)^n \frac{1}{2^n} \sum_{\nu=0}^{\lfloor n/2 \rfloor} \frac{n!}{\nu!(n-2\nu)!} \left(\frac{1}{\sigma_n \sigma_t}\right)^{n-2\nu} \int_{I_k} e^{-x^2/2\sigma_t^2} x^{n-2\nu} dx \quad (C13)$$

and the following function that encapsulates the integral within $\tilde{\chi}$

$$\Lambda_n(k, \gamma) = \int_{I_k} e^{-x^2/\gamma} x^n dx. \quad (\text{C14})$$

We remark that relating the indefinite form of this function to the incomplete gamma function up to a constant term allows for the rapid calculation of Λ for successive values of n using the related recursion relation, which is useful when computing the sum in (C13). The analytic form of Λ for any n can be written as

$$\Lambda_n(k, \gamma) = \begin{cases} -\frac{1}{2} e^{-x^2/\gamma} \sum_{i=0}^m \frac{m!}{(m-i)!} \gamma^{i+1} x^{2m-2i} \Big|_a^b, & m = \frac{n-1}{2}, \text{ if } n \text{ is odd} \\ -\sum_{i=1}^m \frac{1}{2^i} \frac{(2m-1)!!}{(2m-(2i-1))!!} \gamma^i e^{-x^2/\gamma} x^{2m-(2i-1)} + \frac{(2m-1)!!}{2^{m+1}} \sqrt{\pi} \sqrt{\gamma^{2m+1}} \operatorname{erf}(x/\sqrt{\gamma}) \Big|_a^b, & m = n/2, \text{ if } n \text{ is even,} \end{cases} \quad (\text{C15})$$

where a and b are the lower and upper bounds of the interval I_k in the x -quadrature and $n!! := \prod_{k=0}^{\lceil n/2 \rceil - 1} (n - 2k)$. We therefore obtain the following form for the function $\tilde{\chi}_n$ for any n

$$\tilde{\chi}_n(k, \sigma_n^2) = \frac{1}{\sqrt{2\pi}\sigma_t} \left(\frac{\sigma_N}{\sigma_t} \right)^n \frac{1}{2^n} \sum_{\nu=0}^{\lfloor n/2 \rfloor} \frac{n!}{\nu!(n-2\nu)!} \left(\frac{1}{\sigma_n \sigma_t} \right)^{n-2\nu} \Lambda_{n-2\nu}(k, 2\sigma_t^2) \quad (\text{C16})$$

and the generic matrix element of the noisy, discretized measurement operator is given by

$$(\hat{\Sigma}_k)_{\mu, \nu} = \sqrt{\frac{\mu! \nu!}{2^{\mu+\nu}}} \sum_{m=0}^{\lfloor \mu/2 \rfloor} \sum_{n=0}^{\lfloor \nu/2 \rfloor} \frac{(-1)^{m+n} 2^{\mu+\nu-2m-2n}}{m! n! (\mu-2m)! (\nu-2n)!} \tilde{\chi}_{\mu+\nu-2m-2n}(k, \sigma_n^2). \quad (\text{C17})$$

In the special case in which there is zero Gaussian noise, the formula for the matrix elements takes the more straightforward form

$$(\hat{\Sigma}_k)_{\mu, \nu} = \langle \mu | \int_{I_k} |x\rangle \langle x| dx | \nu \rangle = \int_{I_k} \phi_\mu(x) \phi_\nu(x) dx \quad (\text{C18})$$

and examination of the form of the integral allows one to obtain

$$(\hat{\Sigma}_k)_{\mu, \nu} = \sqrt{\frac{\mu! \nu!}{2^{\mu+\nu}}} \sum_{m=0}^{\lfloor \mu/2 \rfloor} \sum_{n=0}^{\lfloor \nu/2 \rfloor} \frac{(-1)^{m+n} 2^{\mu+\nu-2m-2n}}{m! n! (\mu-2m)! (\nu-2n)!} \frac{1}{\sqrt{\pi}} \Lambda_{\mu+\nu-2m-2n}(k, 1). \quad (\text{C19})$$

Appendix D: Comparison of fixed and equal-probability bins

As mentioned in the main text, it is interesting to consider the case in which the ADC bins may be of variable width such that the $p(k|\rho_0)$ are all equal. In the case of homodyne measurements on coherent states, the probability associated with an arbitrary bin is given by (B5). By asserting that all bins $d = 2^\Delta$ are equiprobable for the vacuum input, we find that the interval I_k of the X -quadrature covered by bin k must be given by

$$I_k = \sqrt{2}\sigma_T \left[\operatorname{erf}^{-1} \left(\frac{2k}{d} - 1 \right), \operatorname{erf}^{-1} \left(\frac{2(k+1)}{d} - 1 \right) \right] \quad (\text{D1})$$

with $k \in \{0, \dots, d-1\}$.

In Fig. D.1(a), we show a comparison of the entropy associated with flexible bin widths (dashed lines) and fixed bin widths with a naive choice of $R = 1.5\sigma_v$ (solid lines) with bit depths of $d = 2^2, 2^3$ and 2^4 . In each case, we truncate the Fock space at $N = 30$. The flexible-bin ADC offers a meaningful advantage over its fixed-bin counterpart under the chosen range across most SNRs considered. We also show, for 2^2 bins, the entropy obtained when optimising over the range at each SNR. We find this regime offers marginally higher entropy than the flexible-bins approach at high SNRs. This advantage is likely due to the finite Fock-space cutoff that weighs more heavily on the fixed-bin approach that offers a tunable range parameter that may be used to somewhat mitigate this problem.

In Fig. D.1(b), we compare the entropy of the coherent state protocol with fixed and flexible ADCs. As the coherent state approach requires multiple output distributions, changes to the entropy associated with a flexible- vs fixed-bin ADC are non-trivial. We consider three realisations of the protocol:

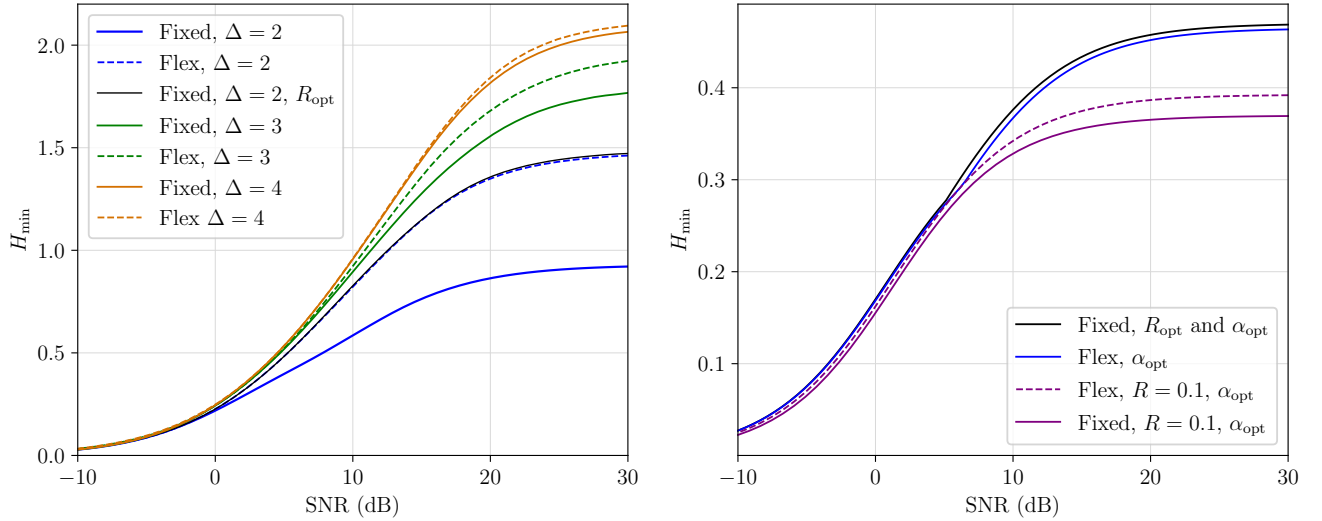


FIG. D.1. Comparison of fixed- vs flexible-bin ADC configurations. Left panel: complete detector characterisation protocol. Right panel: coherent state protocol.

1. A fixed-bin ADC with 2^2 bins. Selecting range $R = R_{\text{opt}}$ and probe state amplitudes $\{0, \alpha_{\text{opt}}\}$ where R_{opt} and α_{opt} are the values of R and α that maximise the rate at any given SNR.
2. A flexible-bin ADC with 2^2 bins and probe state amplitudes $\{0, \alpha_{\text{opt}}\}$
3. A fixed-bin ADC with naive range $R = 1.5\sigma_v$ and probe states $\{0, \alpha_{\text{opt}}\}$
4. A flexible-bin ADC with the same probe states as realisation 3 at each SNR.

In each case we assume ideal parameters $\eta = 1$ and $\gamma = 0$. We find that, at any SNR, there are optimal choices of R and α under which the fixed-bin ADC in scenario (1) outperforms the flexible-bin ADC in scenario (2). Despite this, we find that realisation (4) outperforms realisation (3) for the naive choice of $R = 0.1$ across all SNRs as shown in Fig. D.1(b), and we note that there are several other choices of R for which this is the case. These results suggest that a fixed-bin ADC is optimal if the SNR is known to a good degree of certainty, and the ADC range and coherent state amplitudes can be finely tuned. If any of these conditions are not satisfied, a flexible-bin ADC, offering consistently high entropy under a broad range of parameters, would be preferred.

Appendix E: Considerations regarding implementation of the SDP in practice

Here, we consider the effect of finite-size effects in the observed distributions and the effect of the chosen Fock-space cutoff on the SDP results. We also briefly discuss the software used to obtain our results.

1. Finite-size effects

Any real implementation of our protocol is limited in that the observed average probability distributions and thus the entropy will be computed based on a finite number of samples. In order to incorporate such finite-size effects into our security analysis, we make use of the Chernoff-Hoeffding tail inequality which allows us to quantify the probability that a sum of random variables deviates from its expected value [38]. From the observed data we can obtain distributions of the form $\xi(k|\rho) = \frac{n_k}{\sum_k n_k}$ where n_k is the number of samples measured in bin k from a total of $N = \sum_k n_k$ samples for a given input state ρ . Then using a solution to the dual SDP, we may (neglecting finite-size effects) compute the guessing probability as

$$p_g \leq \bar{p}_g = - \sum_{k=1}^d \sum_{i=1}^n \nu_k^i \xi(k|\rho_i). \quad (\text{E1})$$

The Chernoff-Hoeffding inequality allows us to write an upper bound on the true probability $p(k|\rho)$ of

$$p(k|\rho) \leq \xi(k|\rho) + t \left(\epsilon, \sum_k n_k \right) \quad (\text{E2})$$

where $t(\epsilon, N) = \sqrt{\log(1/\epsilon)/(2N)}$ with ϵ being the probability that the upper bound of (E2) is not satisfied. Using this bound and a choice of ϵ commensurate with the security requirements of the protocol (in our results we choose $\epsilon = 10^{-9}$), we can compute an upper bound on the guessing probability of

$$\bar{p}_g \leq \bar{p}_g^N = - \sum_{k=1}^d \sum_{i=1}^n \nu_k^i \xi(k|\rho_i) + \sum_{k=1}^d \sum_{i=1}^n |\nu_k^i| t \left(\epsilon, \sum_k n_k \right). \quad (\text{E3})$$

2. Fock-space cutoff

In order to implement the SDP (2) in practice, the variables $\{\hat{M}_k^\lambda\}$ must be represented by finite-dimensional matrices. For an optical protocol, it is natural to work in Fock space. However, the coherent states used as probe states in the specific protocol considered here have support on the entire infinite-dimensional space. Hence, a cutoff must be applied.

Each constraint in the last line of the SDP (2) is of the form

$$\langle \alpha | \sum_{\lambda=1}^d \hat{M}_k^\lambda | \alpha \rangle = p(k|\alpha), \quad (\text{E4})$$

for some k, α , and observed distribution $p(k|\alpha)$. Expressing this in the Fock basis we obtain

$$e^{-|\alpha|^2} \sum_{\mu=0}^{\infty} \sum_{\nu=0}^{\infty} \frac{(\alpha^*)^\mu \alpha^\nu}{\sqrt{\mu! \nu!}} \langle \mu | \sum_{\lambda} \hat{M}_k^\lambda | \nu \rangle = p(k|\alpha). \quad (\text{E5})$$

When implementing the SDP in practice, we truncate the infinite sums appearing here by introducing a cutoff N in Fock space

$$e^{-|\alpha|^2} \sum_{\mu=0}^N \sum_{\nu=0}^N \frac{(\alpha^*)^\mu \alpha^\nu}{\sqrt{\mu! \nu!}} \langle \mu | \sum_{\lambda} \hat{M}_k^\lambda | \nu \rangle = p(k|\alpha). \quad (\text{E6})$$

The $\{\hat{M}_k^\lambda\}$ are taken to live in this $N + 1$ dimensional space, and the dimension appearing in (2) then also becomes $D = N + 1$.

The situation differs somewhat in the case of full detector tomography where the constraints are given by

$$\sum_{\lambda=1}^d \hat{M}_k^\lambda = \hat{\Sigma}_k \quad \forall k. \quad (\text{E7})$$

In this case, increasing the space in which the operator on the right-hand side resides imposes additional constraints on Eve's operators in the additional space, and thus the entropy will increase with N and converge when the contribution of the additional constraints becomes negligible. This is in contrast to (E6) where the larger Fock-space cutoff increases the number of terms in the sum on the left-hand side while leaving the right-hand side unchanged. In this case, increasing the Fock-space cutoff past the point at which Eve can reproduce the distributions $\{p(k|\rho_i)\}$ will not increase the entropy.

In the case of complete detector tomography, a valid solution to the SDP can be obtained with $N = 1$ (however, a non-trivial solution requires $N \geq 2$). In contrast, when considering the general approach in which the observed distributions appear in the constraints, the Fock-space cutoff must be sufficiently large to allow the construction of operators on the left-hand side that are physically able to reproduce such distributions, otherwise the SDP becomes infeasible. To illustrate this feature in our coherent-state protocol, we consider the case in which we select one probe state in addition to the vacuum. We then find the maximum amplitude $\alpha_{\max, N}$ of the probe state for which a valid solution to the SDP can be obtained for a given N . Any coherent state with amplitude $\alpha > \alpha_{\max, N}$ is insufficiently supported in the N -dimensional space and thus the SDP is infeasible. We plot this quantity as a function of N in Fig. E.1(a). In Fig. E.1(b), we plot the convergence of the entropy under complete detector tomography with various SNRs. We find that the guessing probability of Eve decreases (the min-entropy increases) monotonically with increasing Fock-space cutoff. Conveniently, this means that a low choice of cutoff does not lead to an overestimation of the randomness.

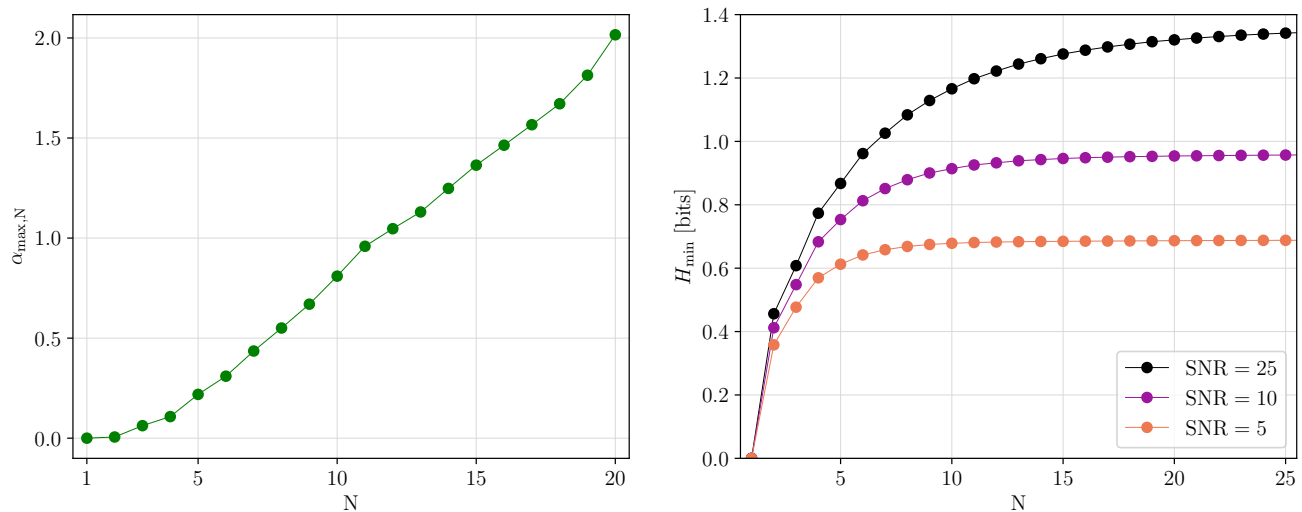


FIG. E.1. Behavior of the protocol with Fock-space truncation. Left: plot of the maximum probe coherent state amplitude $\alpha_{\max,N}$ for which a valid solution to the SDP can be obtained for a given Fock-space cutoff N . Generated using input states with amplitudes $\{0, \alpha_{\max,N}\}$ with $\Delta = 4$, $R = 0$, $\eta = 1$, $\gamma = 0$ and an SNR of 10. Right: convergence of the minimum entropy with Fock-space cutoff in the complete detector tomography case for various SNRs and $\Delta = 4$.

3. Software

For the results throughout this work, all SDPs were implemented in Python using the CVXPY package to express the problem programmatically in a high-level form before obtaining the solution using the MOSEK conic optimization package. Most results were obtained by executing the algorithm on a high-performance computing cluster hosted by the Technical University of Denmark

Appendix F: Experimental setup

Here we present the experimental setup, illustrated in Fig. F.1. A coherent state is generated at a sideband frequency by intensity modulating a seed beam. The amplitude of the coherent state can be controlled by adjusting the peak-to-peak voltage of the signal driving the modulator. The state is measured by homodyne detection, that is locked to the X -quadrature of the seed beam. The lock is implemented using a standard AC locking scheme; the optical local oscillator is phase modulated at 50 kHz by an EOM and the DC signal of the homodyne detector is then downmixed at 50 kHz and lowpass filtered to reveal the error signal. The error signal is then passed to a PID controller that locks the phase of the LO to be in phase with the seed beam and therefore also the coherent sideband state. The AC output of the homodyne detector, carrying the quadrature information of the coherent sideband state is then amplified and bandpass filtered before being digitized by an 16-bit ADC.

1. Digital signal processing chain

Here we describe in detail the four parts of the first block of the digital signal processing (DSP) pipeline. The first part is the digital downmixing of the raw 16-bit homodyne time traces $V(t)$, which in itself consist of three steps: 1) finding the downmixing frequency, 2) finding the downmixing phase and 3) downmixing. The second part is conversion from bit values to quadrature values and the final two parts are estimation of the corresponding amplitudes of the measured coherent probe states and construction of downsampled quadrature distributions to be passed to the SDP protocol.

Fig. F.2 shows plots of the power spectral density (PSD) of the raw time traces. Note that here and below, the data set used for plotting is different from the one in the main text (which contains more datapoints), but the methods and procedures are exactly the same.

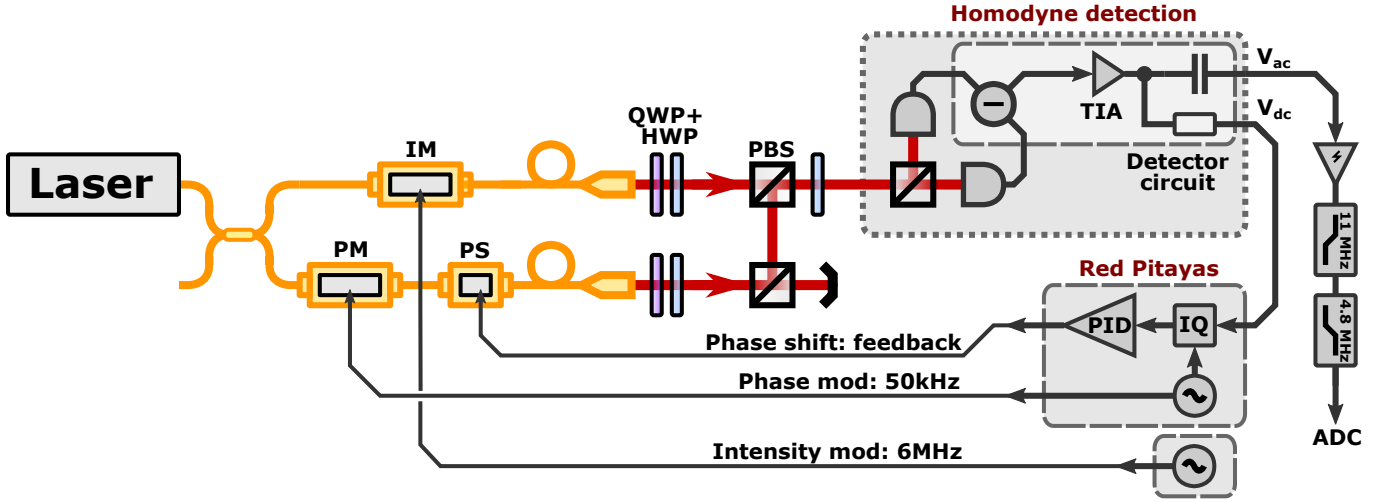


FIG. F.1. Experimental setup to generate and measure a sideband coherent state. The components used are 1550 fiber laser (NKT Photonics Koheras BASIK E15), fiber intensity modulator (IM, iXblue MPZ-LN-10), fiber phase modulator (PM, iXblue MPX-LN-0.1), fiber phase shifter (PS, General Photonics FPS-002), quarter-wave plate (QWP), half-wave plate (HWP), polarization beamsplitter (PBS), polarization based homodyne detector with a trans-impedance amplifier (TIA) stage and AC/DC voltage splitting and an analogue-to-digital converter (ADC, GaGe Razor Express16XX CompuScope PCIe digitizer board).

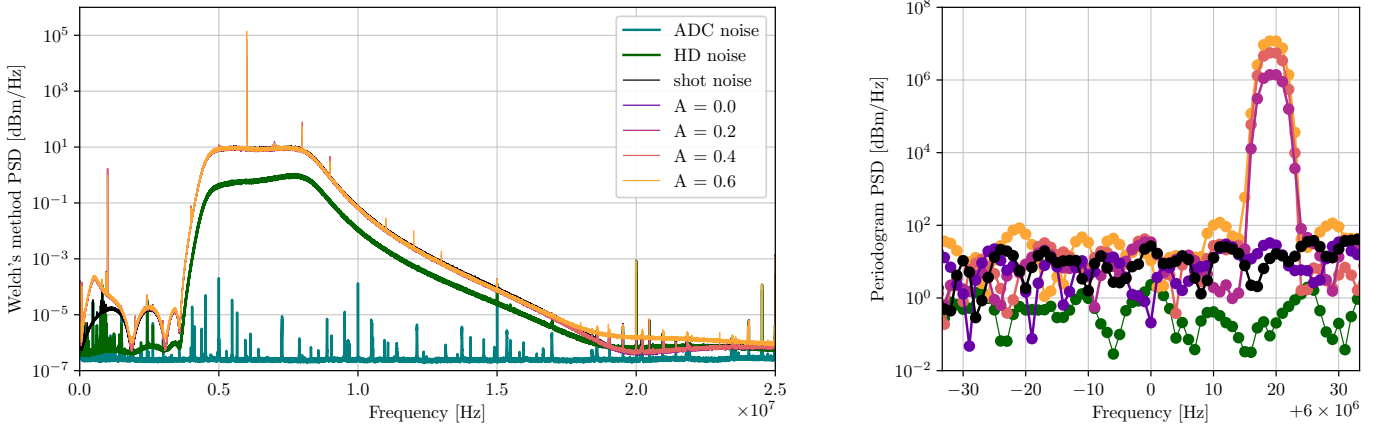


FIG. F.2. (left) PSDs of the raw 16-bit homodyne time traces calculated using Welch's method, including electronic noise traces from the ADC and homodyne detector (HD). Welch's method results in filtered traces that better visualize the structure of the full frequency spectrum. The sideband modulation peak is clearly seen at 6 MHz, together with the bandpass filtering effect of the 11 MHz LPF and 4.8 MHz HPF. (right) Zoom of the PSDs around 6 MHz calculated using periodograms to avoid any filtering of the peak structure. The peak height is seen to correlate correctly with the modulation strength and that there is a sufficient clearance to the HD noise floor.

2. Digital downmixing

Downmixing is typically performed in the electrical domain by mixing the signal with a corresponding electrical modulation signal followed by low-pass filtering (LPF) in order to convert the sideband signal to a dc value. In the digital domain the process is similar and the downmixed time traces are calculated as follows:

$$v_{dm}(t) = f_{lpf} [v(t)\Re(v_{dlo}(t))] + i f_{lpf} [v(t)\Im(v_{dlo}(t))] \quad (F1)$$

where $v(t)$ is the input signal, $v_{dlo}(t) = e^{i(2\pi t f_{dlo} + \phi_{dlo})}$ is the digital local oscillator (DLO) and f_{lpf} is a filter function that implements a linear digital filter twice, once forward and once backwards, using a 501th-order low pass finite impulse response (FIR) filter with a cutoff frequency of $f_c = 1$ MHz. Both f_{lpf} and the FIR filter are implemented with the `scipy.signal` python package using the `filtfilt` and `firwin` functions, respectively. But before the downmixing can be performed we first need to determine the proper frequency f_{dlo} and phase ϕ_{dlo} of the DLO.

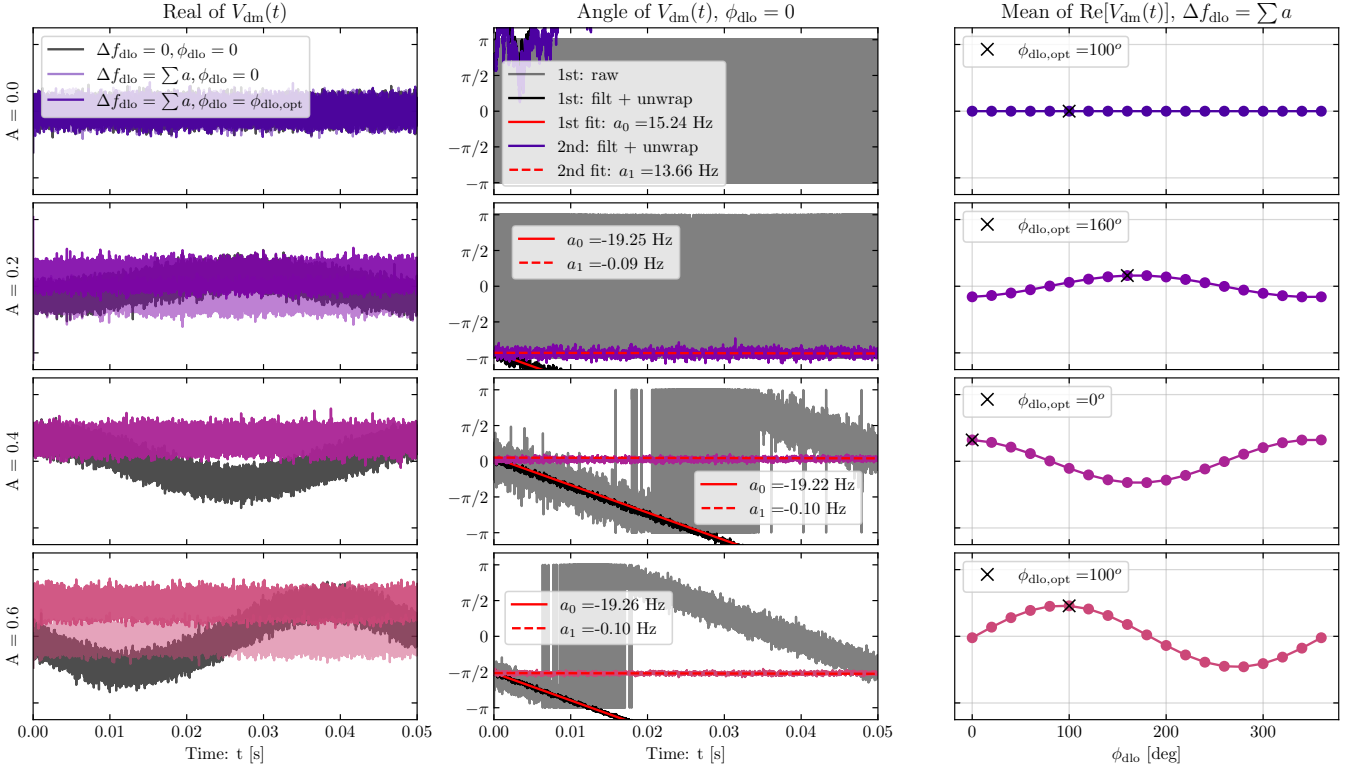


FIG. F.3. Overview of the steps involved in the digital downmixing procedure.

a. Finding the DLO frequency offset: Δf_{dlo}

Even though we set the function generator to provide a $f_{\text{mod}} = 6$ MHz signal to the amplitude modulator the actual frequency of the optical signal will vary slightly. We therefore need to find the frequency offset Δf_{dlo} needed to adjust the DLO to match the actual frequency of the optical signal. This offset can be estimated by fitting the evolution of the angle of the complex valued $v_{dm}(t)$, as the frequency mismatch between the DLO and signal will result in a constant phase drift of the downmixed signal. A visualization of this is shown in Fig. F.3. Here the left column show the drift of the downmixed signal (in grey) when $f_{dlo} = f_{\text{mod}}$, the center column shows the corresponding angle (in grey) of $V_{dm}(t)$, which after filtering and unwrapping can be fitted with $at + b$. A new downmixed signal is then calculated with $f_{dlo} = f_{\text{mod}} + \Delta f_{dlo}$, where $\Delta f_{dlo} = a_0$ and from that trace a second smaller correction term a_1 is estimated. The process is repeated n times with $\Delta f_{dlo} = \sum_n a_n$ until the resulting phase drift is fully eliminated ($a_n \approx 0$). The result of this intermediate step is represented by the transparent traces in the left column of Fig. F.3. We note that for our data, only a single step was required as $a_1 \approx 0$ for all probe states and that the same DLO offset could be obtained independent of the chosen DLO phase.

b. Finding the optimal downmixing phase: $\phi_{dlo,opt}$

Using the correct DLO frequency will result in a downmixed time trace of constant mean value. This value then depends on the phase of the DLO, ϕ_{dlo} , relative to the signal. We therefore need to find the $\phi_{dlo,opt}$ that maximizes the obtained mean value of the downmixed time trace. This can be done by either a simple brute force search or optimization routine. Such a search is shown in the right column of Fig. F.3 and the resulting proper downmixed signals as the slightly transparent traces in the left column. It is worth noting that shifting $\phi_{dlo,opt}$ by 180° then corresponds to having measured the same probe state with the phase between the optical LO and probe state rotated by 180° .

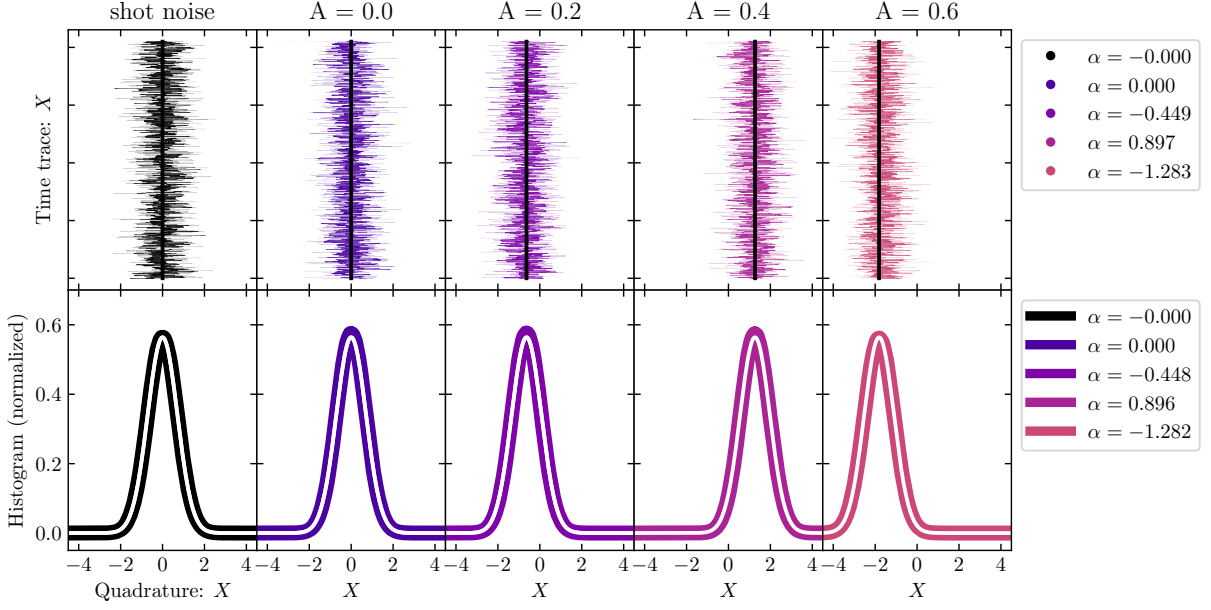


FIG. F.4. **(top row)** Normalized downmixed time traces. The vertical black lines indicate the position of the mean and its value is given by legend. **(bottom row)** X -quadrature distributions of the measured probe states calculated as normalized 500 bin histograms in the quadrature range $[-5, 5]$. The white/black lines indicate the best fit of $\text{Pr}_\alpha(x)$ to the histogram data and the corresponding amplitude is given by the legend.

3. Bit-to-quadrature value conversion

In order to convert the unit of time traces from bits (or voltage) into quadrature values, the trace is normalized against the shot noise level (SNL). A normalized time trace is therefore calculated as $\hat{x} = V(t)/(\sqrt{2}V_{\text{snl}})$, where V_{snl} is the SNL and is obtained as the standard deviation of the shot noise trace. Using this normalization the variance of the shot noise trace becomes equal to the vacuum variance $\langle \Delta \hat{x}_{\text{sn}}^2 \rangle = 1/2$. The normalization of the downmixed traces is then naturally performed using the SNL of the corresponding downmixed shot-noise trace and the result is shown in the upper row of Fig. F.4.

4. Estimation of probe state amplitudes

Given the normalization and that we employ coherent states of real amplitude only, the amplitude α of any such state is equal to the average quadrature value corresponding to taking the mean of the normalized downmixed time trace: $\alpha = \langle \hat{x} \rangle$. Alternatively, using a model of the expectation value of a coherent state $\text{Pr}_\alpha(x) = \pi^{-1/2} e^{-(x-\sqrt{2}\alpha)^2}$, the value of alpha that best fits the measured quadrature distribution (histogram of \hat{x} values) is found. The result of both methods are shown in Fig. F.4 and show good agreement.

5. Downsampling

The ADC we have used in our setup has a depth of 16 bits. However, solving the SDP with 2^{16} constraints for each probe state would require a prohibitive runtime even with generous computational resources. Moreover, as shown in the main text, increasing the bit depth offers little improvement to the extractable randomness after the bit depth exceeds $\Delta = 4$ under realistic parameters. Therefore, we perform downsampling in order to create new histograms with a smaller bit depth over an adjustable range less than the experimental range of the ADC and thus we can solve the SDP rapidly with little reduction in the output entropy.

To illustrate the downsampling procedure, we consider bit depths of $\Delta = 4, 6$ and 8 and quadrature ranges of $R = 1.5, 2.0, 2.5$ and 3.0 . The normalized downmixed traces are binned under the definition of the ADC bin function given by (5) in the main text for a given R and Δ . The downsampled histograms are shown in Fig. F.5. Bin frequencies

are presented as points plotted at the center of all interior bins while points at $-R$ and R show the frequencies of the end bins at the lower- and upper-end of the range, respectively. The percentage of the total data points that fall into either of the end bins is shown for each dataset on the right-hand side for each R and is independent of the chosen bit depth.

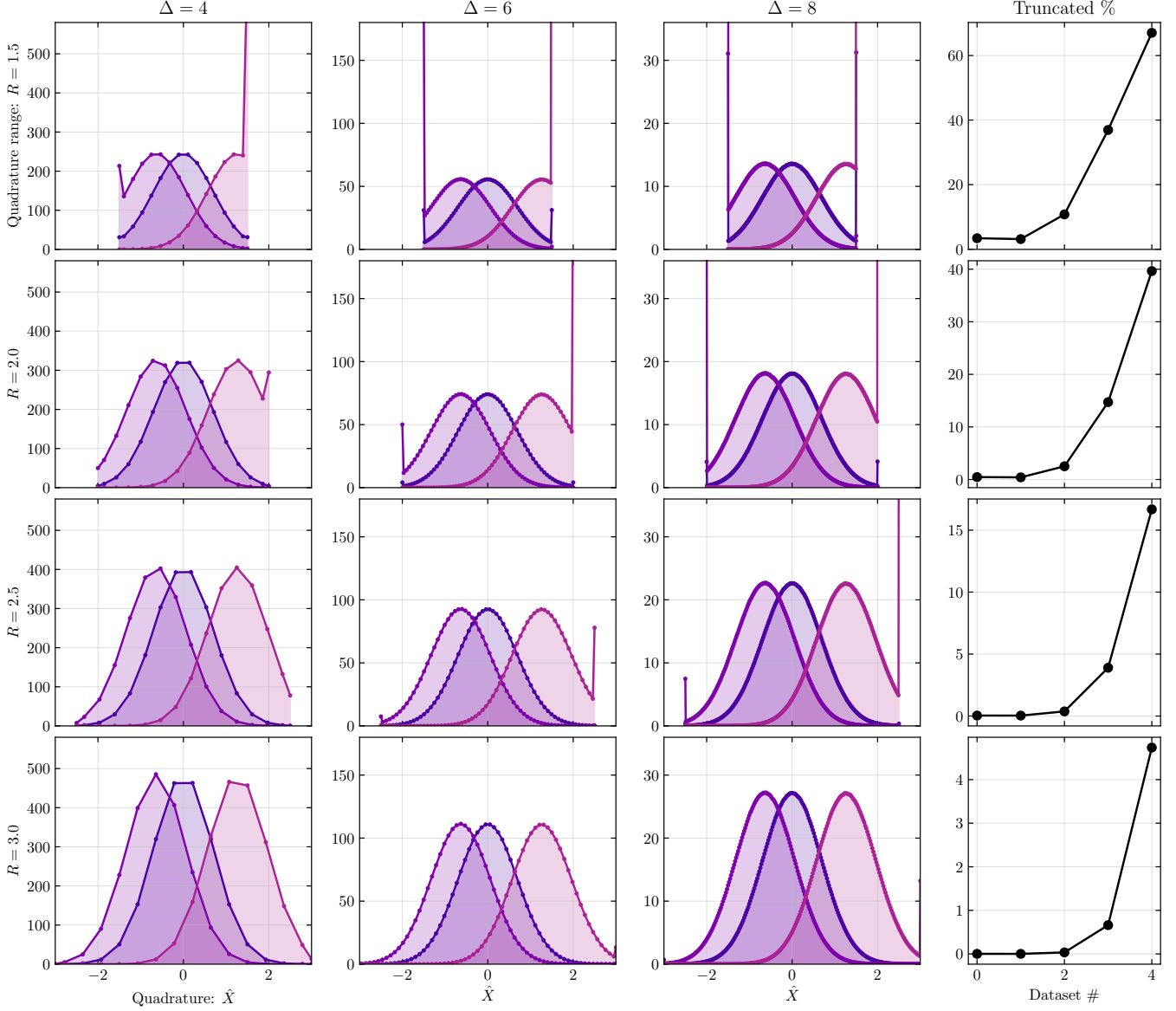


FIG. F.5. Histograms of downsampled versions of the normalized downmixed time traces from the top row of Fig. F.4. The y-axis of the histograms corresponds to bin counts $\times 10^5$. The percentage of data points truncated by the corresponding downsampling is shown in the rightmost plots, with data set number corresponding to the sequence [shot noise, $A = 0.0$, $A = 0.2$, $A = 0.4$, $A = 0.6$].

Appendix G: Effect of amplitude estimation errors

In any experimental implementation, there is necessarily some uncertainty in the amplitudes of the trusted probe states. As the probe states are assumed to be known in the min-entropy certification step, such uncertainties may, in principle, compromise the protocol's security, i.e. lead to overestimation of the entropy.

Intuitively, if actual probe states are more distinguishable than assumed, Eve can cheat. Indeed, if the probe states are perfectly distinguishable, Eve can cheat by first identifying the state and then outputting according to any local

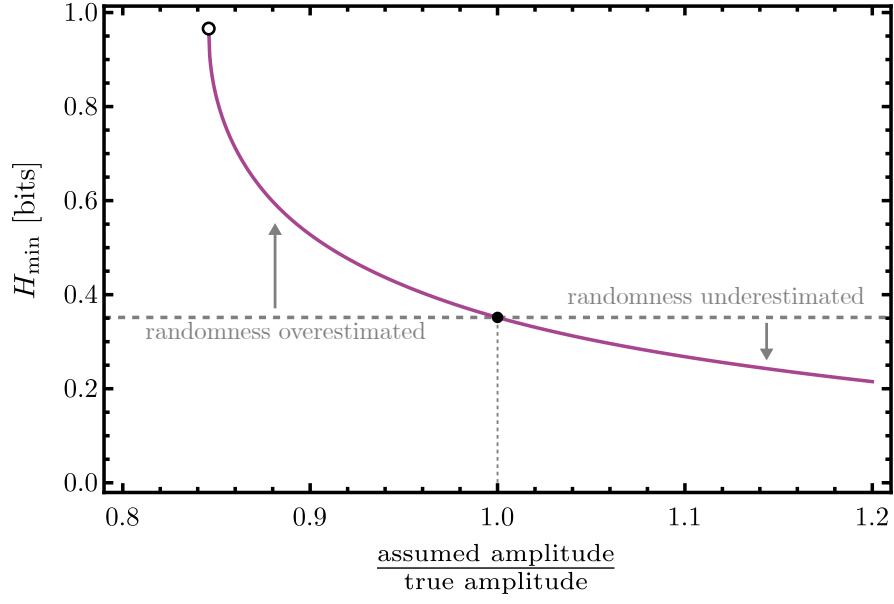


FIG. G.1. Min-entropy (as computed via (2)) vs. amplitude estimation error, for the coherent-state protocol using four states with amplitudes $\alpha_0 = 0$, $\alpha_1 = 0.33$, $\alpha_2 = 0.66$, $\alpha_3 = 1.0$, and $\Delta = 2$, $R = 1.5$, $\gamma = 0$, $\eta = 1$, and an SNR of 15 dB. The filled circle and horizontal, dashed line indicate the true value of H_{\min} corresponding to no estimation error. To the left of the open circle, the SDP becomes infeasible (it becomes impossible to reproduce the true distributions by measurements on the less distinguishable assumed coherent states).

probability distribution she likes. The constraints (in the SDP) that the observed distributions must be reproduced do not then constrain her measurement in the generation rounds in any way, and there is no randomness relative to Eve.

In Fig. G.1, we investigate the effect of the discrepancy between the assumed and true probe-state amplitudes. We fix the values of the true amplitudes that enter in the distributions $p^\gamma(k|\alpha)$ which appear on the right-hand side of the SDP constraints in (2). We then vary the assumed amplitudes which enter on the left-hand side of the same constraints. We take all the amplitudes to be off by the same factor, i.e. we take $\alpha_i^{\text{assumed}} = r\alpha_i^{\text{true}}$ for all i and vary r . The plot shows the min-entropy as computed via the SDP vs. the scaling factor.

We see that, as expected based on the intuition above, overestimation of the amplitudes leads to underestimation of the entropy. In this regime, the protocol is thus still secure, but sub-optimal. Underestimating the amplitudes, however, leads to an overestimation of the entropy, compromising security. Hence, to ensure that amplitude estimation uncertainty does not lead to security holes, one should pick assumed values for the SDP which err to the side of larger values with respect to the estimation.